

Manuscript Number: A-13-858R2

Title: Microscopic mechanism of plastic deformation in a polycrystalline Co-Cr-Mo alloy with a single hcp phase

Article Type: Full Length Article

Keywords: cobalt-chromium-molybdenum alloy, deformation mode, dislocation slip, crystal plasticity analysis, geometrically necessary dislocations

Corresponding Author: Dr. Hiroaki Matsumoto, Ph.D

Corresponding Author's Institution: Kagawa university

First Author: Hiroaki Matsumoto, Ph.D

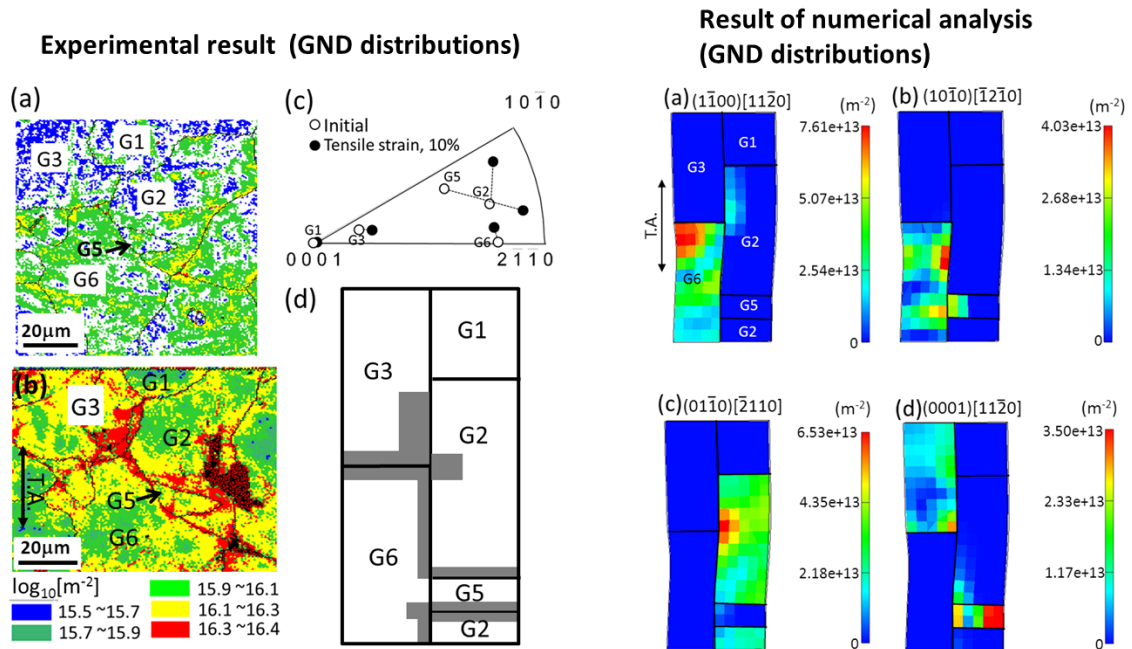
Order of Authors: Hiroaki Matsumoto, Ph.D; Yuichiro Koizumi; Tetsuya Ohashi; Byong-Soo Lee; Yunping Li; Akihiko Chiba

Abstract: A Co-Cr-Mo alloy with a single ϵ (hcp) phase exhibits excellent tensile properties with a 0.2% proof stress of 630 MPa, an ultimate tensile stress of 1072 MPa, and an elongation to fracture of 38.3%. The dominant deformation modes are basal $\langle a \rangle$ slips and prismatic $\langle a \rangle$ slips, and the respective critical resolved shear stresses at room temperature are calculated to be 184 MPa and 211 MPa. This simultaneous activation of both $\langle a \rangle$ slips is explainable with respect to the lattice constant ratio c/a of 1.610. There is a tendency for the geometrically necessary dislocations (GNDs) to accumulate at grain boundaries, and the magnitude of this GND accumulation at a particular boundary is dependent on its character. Numerical analysis using a dislocation-model-based strain gradient crystal plasticity calculation makes it possible to characterize the distributions of dislocation density, local stress, and local strain in the polycrystalline ϵ Co-Cr-Mo alloy, and the calculation is largely consistent with the experimental results. This simulation reveals that the activity of the prismatic $\langle a \rangle$ slips in addition to the basal $\langle a \rangle$ slips contributes to the stress relaxation at the boundary. For this reason, excellent tensile ductility is obtained in the polycrystalline ϵ Co-Cr-Mo alloy.

Cover letter

It is a resubmission of a previously rejected paper.

This article presents the deformation mode of a Co-Cr-Mo alloy with a single hcp phase on the basis of experimental analysis and numerical analysis using a dislocation-model-based strain gradient crystal plasticity calculation. Experimentally, we found that the dominant deformation modes are basal $\langle a \rangle$ slips and prismatic $\langle a \rangle$ slips, and the respective critical resolved shear stresses at room temperature are calculated to be 184 MPa and 211 MPa. This simultaneous activation of both $\langle a \rangle$ slips is explainable with respect to the lattice constant ratio c/a of 1.610. Numerical analysis makes it possible to characterize the distributions of dislocation density, local stress, and local strain in the polycrystalline ϵ Co-Cr-Mo alloy, and the calculation is largely consistent with the experimental results. This simulation reveals that the activity of the prismatic $\langle a \rangle$ slips in addition to the basal $\langle a \rangle$ slips contributes to the stress relaxation at the boundary. For this reason, excellent tensile ductility is obtained in the polycrystalline ϵ Co-Cr-Mo alloy.



I sincerely appreciate your apt indication. As following your comment, I have revised the manuscript as follows.

- (1) As following your comment, I changed “slips” into “slip” in all sentence.
- (2) On page 5 at last sentence (in main text), I have changed the sentence into “This effect indeed supports the possible promotion.”.
- (3) In order not to confuse about expression of strain, I have corrected the sentence as follows.
“There are only four independent strain components caused by activation of basal <a> slip and prismatic <a> slip.” (Line 1-2 in chapter 3-3-1.)
- (4) As following your indication, I have corrected the “slips systems” into “slip systems”.
- (5) In order to make it clear for explaining the Figure 8(a), I have changed the sentence as follows.
“In order to understand the distributions of simulated GNDs more clearly, the results of Figs. 7(a)-(d) are summarized in one figure of Fig. 8(a). In Fig. 8(a), the respective simulated result (in Figs. 7(a)-(d)) is drawn in the experimental result of Fig. 5(d).” (line 18-20, in chapter 3-3-2-3. Dislocation accumulation and distributions of local stress and local strain (experimental and numerical results))
- (6) As following your indication, I have changed the sentence as follows.
“These results indicate that the activity of prismatic <a> slip in addition to basal <a> slip would contribute to the stress relaxation at the boundaries, resulting in the excellent tensile ductility in the ϵ -CCM alloy.” (last sentence in chapter 4. Summary)

Microscopic mechanism of plastic deformation in a polycrystalline Co-Cr-Mo alloy with a single hcp phase

Hiroaki Matsumoto¹, Yuichiro Koizumi², Tetsuya Ohashi³, Byong-Soo Lee², Yunping Li², Akihiko Chiba²

1. Department of Advanced Materials Science Faculty of Engineering, Kagawa University, 2217-20 Hayashi-cho, Takamatsu, Kagawa 761-0396, Japan
2. Institute for Materials Research, Tohoku University, 2-1-1 Katahira, Aoba-ku 980-8577, Japan
3. Kitami Institute of Technology, Koencho 165, Kitami 090-8507, Japan

Abstract

A Co-Cr-Mo alloy with a single ϵ (hcp) phase exhibits excellent tensile properties with a 0.2% proof stress of 630 MPa, an ultimate tensile stress of 1072 MPa, and an elongation to fracture of 38.3%. The dominant deformation modes are basal $\langle a \rangle$ slip and prismatic $\langle a \rangle$ slip, and the apparent respective critical resolved shear stresses at room temperature are calculated to be 184 MPa and 211 MPa. This simultaneous activation of both $\langle a \rangle$ slips is explainable with respect to the lattice constant ratio c/a of 1.610. There is a tendency for the geometrically necessary dislocations (GNDs) to accumulate at grain boundaries, and the magnitude of this GND accumulation at a particular boundary is dependent on its character. Numerical analysis using a dislocation-model-based strain gradient crystal plasticity calculation makes it possible to characterize the distributions of dislocation density, local stress, and local strain in the polycrystalline ϵ Co-Cr-Mo alloy, and the calculation is largely consistent with the experimental results. This simulation reveals that the activity of the prismatic $\langle a \rangle$ slip in addition to the basal $\langle a \rangle$ slip contributes to the stress relaxation at the boundary. For this reason, excellent tensile ductility is obtained in the polycrystalline ϵ Co-Cr-Mo alloy.

Key words: cobalt-chromium-molybdenum alloy, deformation mode, dislocation slip, crystal plasticity analysis, geometrically necessary dislocations

1. Introduction

Cobalt-chromium-molybdenum (Co-Cr-Mo, hereafter designated as CCM) alloys have been used in various medical applications because of their excellent biocompatibility and mechanical properties [1-2]. The ternary phase diagram of Co-Cr-Mo alloy in the

practically used compositional region reveals that the equilibrium phases are γ (face-centered cubic, fcc), ϵ (hexagonal close packed, hcp), and σ (CoCr, $P42/mnm$). A massive transformation from the supersaturated γ phase is found to result in the formation of a single ϵ phase in Co-(27–29 mass%)Cr-(5–6 mass%)Mo alloy [3]. Therefore, a single ϵ phase can be obtained without σ precipitation using an optimal thermomechanical process inducing this massive transformation in Co-27%Cr-5%Mo alloy. Quite recently, the authors have reported that a Co-27%Cr-5%Mo alloy consisting of a single hcp structure exhibits both high strength and excellent tensile ductility along with a plastic elongation of more than 30%. In this investigation, the simultaneous activation of both the basal $\langle a \rangle$ slip and prismatic $\langle a \rangle$ slip was also noted [4]. The ϵ phase in the CCM alloy is reported to improve its wear properties [1]. Therefore, there is a possibility that a CCM alloy with this ϵ microstructure can be further functionalized for use in biomedical metallic implants. This work aims at examining the basic properties of the deformation behavior of CCM alloys consisting of a single ϵ phase based on experimental and computationally simulated results.

2. Experimental procedures

An ingot of Co-27Cr-5Mo (in mass%) alloy with chemical compositions of 27.1 mass% Cr, 5.03 mass% Mo, N and O with less than 0.01 mass% and balance Co was produced using a vacuum-induction melting furnace. After a homogenization treatment at 1523 K for 21.6 ks, the homogenized ingot was isothermally hot-forged at 1373 K to achieve a reduction in height of 87 %, after which it was furnace-cooled to room temperature to yield an alloy consisting of a single ϵ phase. A tensile test was carried out at an initial strain rate of $1.5 \times 10^{-4} \text{ s}^{-1}$ at room temperature. The deformed microstructure was identified by conducting electron backscatter diffraction (EBSD) analysis and transmission electron microscopy (TEM) observation. The EBSD analysis was conducted using a Philips XL30 FEG SEM equipped with an orientation imaging microscope (OIM) produced by TexSEM Laboratories. The density of geometrically necessary dislocations (GNDs) was calculated from the EBSD data following the procedure reported by Calcagnotto et al. [5] (see details in section 3-3-1). Furthermore, in order to characterize the dislocation accumulation at the grain boundaries, numerical analysis was carried out using a dislocation-model-based strain gradient crystal plasticity calculation (see details in sections 3-3-2-1 and 3-3-2-2) [6-10].

3. Results and discussion

3-1. Microstructure

Figure 1(a) shows the EBSD image quality (IQ) map and inverse pole figure showing the crystallographic orientations with respect to the direction perpendicular to the microstructure (EBSD-IQ image) of the as-hot-forged CCM alloy. This image shows that an equiaxed grained microstructure was formed with an average grain size of 42 μm and random crystallographic orientations. Furthermore, this as-forged microstructure is found to comprise a single ϵ (HCP) phase according to the EBSD analysis and XRD profile. Hereafter, this hot-forged CCM alloy is designated as the ϵ -CCM alloy.

3-2. Plastic deformation at room temperature

3-2-1. Stress-strain curve

The nominal stress–nominal strain curve for tensile deformation is shown in Figure 1(b). The 0.2% proof stress is 630 MPa, and augmented work hardening was associated with increasing strain. Failure occurs at a plastic elongation of 38.3%, and it occurs catastrophically with a very little local necking even though the ϵ -CCM alloy exhibits excellent tensile ductility. As compared to the strength and ductility of a CCM alloy consisting of a γ (fcc) phase [11], a higher strength and a similar excellent ductility are observed for the present ϵ -CCM alloy.

3-2-2. Dislocation slip

Figure 1 shows the EBSD IQ maps of the ϵ -CCM alloy at tensile strains of (a) 0% and (c) 6%. Striations corresponding to slip lines or twinning traces appeared in all grains after deformation. There were no misorientations observed among these striations in the grain, indicating that the striations appeared only through the formation slip lines. Trace analysis of these striations reveals that almost all striations lie along the (0001) (basal) or $\{1\bar{1}00\}$ (prismatic) planes, indicating that two types of slip systems are dominant: basal slip and prismatic slip. In fact, the simultaneous activations of basal $\langle a \rangle$ slip and prismatic $\langle a \rangle$ slip are already observed at strains of 1.3 % and 3 % (corresponding to strains just after yielding). Figures 2(a-c) show the inverse pole figures including the counters denoting the Schmid factor (μ) of (a) basal $\langle a \rangle$ slip and (b) prismatic $\langle a \rangle$ slip along with (c) the ratio of these Schmid factors for the basal $\langle a \rangle$ slip and prismatic $\langle a \rangle$ slip. A ratio of 1.0 means that the μ values for basal $\langle a \rangle$ slip and for prismatic $\langle a \rangle$ slip are equal, and a ratio of more than 1.0 means that μ is higher for basal $\langle a \rangle$ slip. The tensile orientations and the results of the trace analysis for the 32 grains (Fig. 1(c)),

which together distinguish whether the slip line lies on a basal plane or prismatic plane, are also included in Fig. 2(c). Figures 2(d), 2(e), and 2(f) show example images after trace analysis of the slip planes of a sample deformed at 6%. In these figures, we can clearly identify whether the slip lines are lying on the basal plane or prismatic plane or both. From the summary of the trace analysis in Fig. 2(c), it can be noted that interestingly, the two slip modes are almost equally dominant, meaning that basal slip and prismatic slip activate with similar ease during deformation. Figure 3(a) presents a TEM bright-field image showing the dislocation substructure in a grain with a tensile orientation close to $[10\bar{1}0]$ after tensile deformation at a strain of 6%. This photograph was taken with the incident beam parallel to the $\langle\bar{1}2\bar{1}0\rangle$ direction of the sample. Under this condition, the (0001) basal plane and $(10\bar{1}0)$ prismatic plane are aligned parallel to the direction of the incident beam, which allows them to be seen edge-on. The traces of (0001) and $(10\bar{1}0)$ are also shown in Fig. 3(a). Based on the $g \cdot b$ criterion, the dislocations visible in Fig. 3(a) are confirmed to be of the $\langle a \rangle$ type. There are two types of slip systems visible in Fig. 3(a), prismatic $\langle a \rangle$ slip and basal $\langle a \rangle$ slip, and the dislocations are found to be frequently cross-slipping between the prismatic plane and basal plane. Furthermore, glide bands of dislocations are also seen on the prismatic plane, indicating that in the dominant prismatic $\langle a \rangle$ slip mode in the grain in Fig. 3(a), slip proceeds in a relatively planar manner. A tensile orientation close to $[10\bar{1}0]$ means that μ is higher for prismatic $\langle a \rangle$ slip than for basal $\langle a \rangle$ slip. Therefore, we can speculate the critical resolved shear stress (CRSS) of prismatic $\langle a \rangle$ slip is higher than that of basal $\langle a \rangle$ slip. With respect to the activation of $\langle c + a \rangle$ slip, the glide plane for $\langle c + a \rangle$ dislocation is dependent on the lattice constant ratio c/a . The typical glide planes for $\langle c + a \rangle$ dislocations are $\{1\bar{1}01\}$ and $\{11\bar{2}2\}$ [12]. In pure Co, which has a c/a ratio of 1.624, the glide plane for $\langle c + a \rangle$ dislocations is $\{11\bar{2}2\}$. In contrast, in the ϵ -CCM alloy, there are no slip traces in the $\{1\bar{1}01\}$ and $\{11\bar{2}2\}$ planes in Fig. 1(c), indicating that $\langle c + a \rangle$ slip are rarely activated in the ϵ -CCM alloy.

Next, we discuss the CRSS values of basal $\langle a \rangle$ slip and prismatic $\langle a \rangle$ slip in the ϵ -CCM alloy. The starting microstructure before the tensile test has random crystallographic orientations (Fig.1 (a)). Moreover, there is the simultaneous activation of basal $\langle a \rangle$ slip and prismatic $\langle a \rangle$ slip just after yielding. Therefore, the apparent CRSS are roughly calculated using the 0.2% proof stress of 630 MPa in Fig. 1(b) and the average Schmid factor in grains in microstructure of Fig. 1(a). The EBSD analysis (TSL OIM analysis 5) reveals that the average Schmid factors (μ) of basal $\langle a \rangle$ slip and prismatic $\langle a \rangle$ slip in microstructure of Fig. 1(a) are 0.292 and 0.335, respectively. So, the apparent CRSS values of basal $\langle a \rangle$ slip and prismatic $\langle a \rangle$ slip according to the

0.2% proof stress of 630 MPa (Fig. 1(b)) can be roughly estimated to be 184 MPa and 211 MPa, respectively. These values are almost consistent with the CRSS which was identified by mechanical testing using the single-crystal-samples of ϵ -CCM alloy [13].

It is well known that active slip systems in hcp metals are correlated with the c/a ratio [12]. This phenomenon has been observed previously in relation to calculations of the Peierls stresses [14], calculations based on lattice dynamics [15], and the ease of the hcp transformation [16]. In pure Co, which has a c/a of 1.624 ($a = 2.506 \text{ \AA}$, $c = 4.071 \text{ \AA}$) according to Ref.[17] and 1.628 according to Ref. [12], the primary slip system is basal $\langle a \rangle$ slip. The lattice constants of the present ϵ -CCM alloy measured by the XRD analysis are 2.53 \AA on the a -axis and 4.078 \AA on the c -axis, and the c/a is therefore 1.610. The c/a (1.624) of pure Mg is similar to that of pure Co. Single-crystal studies of Mg alloys have shown that the CRSS for nonbasal $\langle a \rangle$ slip is considerably higher than that for basal $\langle a \rangle$ slip [18]. The ease of prismatic $\langle a \rangle$ slip activity in the vicinity of grain boundaries in the polycrystalline Mg alloy AZ31 has been reported by Koike et al. [19] and was attributed to large accumulations of grain-boundary compatibility stress. However, since depending on Schmid factor, prismatic $\langle a \rangle$ slip is activated without basal $\langle a \rangle$ slip in the present ϵ -CCM alloy, as shown in Fig. 2(e), indicating that the prismatic $\langle a \rangle$ slip is not activated due to the grain-boundary compatibility stress. According to a previous summary of the relationship between c/a and the activation of slip modes in hcp metals [12], the principal $\langle a \rangle$ slip plane generally changes from the prismatic to the basal plane at c/a ratios between 1.593 and 1.615. Hauser et al. reported that addition of Li into Mg decreases c/a to approximately 1.607, which is close to that in the present ϵ -CCM alloy [20]. Hauser et al. has also pointed out the frequent occurrence of prismatic $\langle a \rangle$ slip after c/a has decreased to 1.607 in the Mg-Li alloy [20]. This change is primarily associated with a decrease in the (0002) lattice spacing rather than an increase in the $\{10\bar{1}0\}$ planar spacing. Hence, the decrease in the c/a to 1.593–1.615 is thought to lead to an increase in the Peierls stress for basal slip relative to that for prismatic slip. Therefore, we can simply explain the simultaneous activity of both basal $\langle a \rangle$ and prismatic $\langle a \rangle$ slip systems in the present ϵ -CCM alloy in relation to the Peierls stress associated with the c/a value of 1.610.

In addition, there are other considerations related to the activity of nonbasal $\langle a \rangle$ slip in basal-slip-dominated hcp metals such as Mg and Be [21-23]. In particular, such nonbasal slip is found to be better understood as thermally activated “cross slip” of basal dislocations, since $\langle a \rangle$ dislocations prefer to dissociate into Shockley partial dislocations lying in the basal plane. Furthermore, Agnew et al. pointed out one possible reason why nonbasal slip frequently activates in Mg-Li alloys (hcp): the addition of Li

into Mg increases the effective stacking-fault energy (SFE) of the basal stacking faults [24]. This effect indeed supports the possible promotion of prismatic cross-glide of $\langle a \rangle$ dislocations. The SFE of pure Co at room temperature is approximately 31 mJ m^{-2} , which is the lowest SFE value among all the hcp metals [17]. The SFE at room temperature calculated by Thermo-Calc is approximately 0 mJ m^{-2} for pure Co and 117 mJ m^{-2} for the present ϵ -CCM alloy, indicating that addition of Cr or Mo into Co leads to an increase in the SFE of the hcp phase. Therefore, there is also a possibility that the frequent occurrence of prismatic $\langle a \rangle$ slip in the ϵ -CCM alloy can be explained in relation to the increase in SFE.

3-2-3. Deformation twinning

It has long been recognized that deformation twinning plays an important role in the deformation of hcp metals because of their limited dislocation slip systems [25-27]. The frequent activation of deformation twins in pure polycrystalline Co during deformation has been reported by Zhang et al., who found that tension twins on the $\{10\bar{1}2\}$ plane constitute the predominant proportion of the twins (approximately 82.1%) [28]. In contrast, the frequent occurrence of deformation twins in the ϵ -CCM alloy with tensile strains between 0% and 10% cannot be confirmed by the EBSD analysis and TEM observations. In fact, several twins are seen after fracture with a strain of 38%, but only in grains with a tensile orientation close to $[0001]$, corresponding to the hard orientation for both $\langle a \rangle$ slips on the basal plane and those on the prismatic plane (Figs. 3(b) and 3(c)). Here, the twinning systems in Fig. 3(c) are identified by EBSD-analysis-software (TSL OIM Analysis 5). Many kinds of twins on the $\{11\bar{2}1\}$, $\{10\bar{1}2\}$, $\{10\bar{1}3\}$, and $\{11\bar{2}2\}$ planes are found to be activated in grains with tensile orientations close to $[0001]$, as shown in Fig. 3(c). According to the orientation dependence of twinning in hcp metals ($c/a < \sqrt{3}$) under tension and compression [29], the activation of $\{11\bar{2}1\}$, $\{10\bar{1}2\}$, and $\{11\bar{2}2\}$ twins in grains with tensile axes close to $[0001]$ can be reasonably explained. This result indeed means that twinning does not activate frequently, and the CRSS for twinning is extremely high in the present ϵ -CCM alloy.

The abovementioned results indicate that dominant deformation modes of pure Co and the ϵ -CCM alloy are different. Deformation twins and basal $\langle a \rangle$ slip comprise the dominant modes for pure Co, whereas the simultaneous activation of basal $\langle a \rangle$ slip and prismatic $\langle a \rangle$ slip constitutes the dominant mode for ϵ -CCM alloy. Zhang et al. mentioned that frequent occurrence of deformation twins and the simultaneous activation of tension and compression twins in the same grain of pure Co can be

attributed to its low SFE [28]. Unfortunately, the specific SFE values for each crystallographic plane in the ϵ -CCM alloy are not yet understood. However, the drastic decrease in the occurrence of deformation twins and the enhancement of prismatic $\langle a \rangle$ slipping in the ϵ -CCM alloy as compared with pure Co should be related to the different SFE values of the hcp phase at room temperature (117 mJ m^{-2} for the present ϵ -CCM alloy and 0 mJ m^{-2} for pure Co, as calculated by the Thermo-Calc software).

3-2-4. Fracture behavior

Figures 4(a) and (b) present SEM images ((a) lower magnification and (b) higher magnification) showing the fracture surface after deformation of the ϵ -CCM alloy at a strain of 38 %, where there are mixtures of flat regions and dimple-like regions. The cleavage fracture surface can be clearly seen in the flat region in Fig. 4(b), indicating that fracture frequently occurs at the grain boundary. Therefore, the catastrophic fracture after tensile deformation of the ϵ -CCM alloy is found to comprise both brittle grain-boundary fracture and dimple fracture occurring inside the grain. In the ϵ -CCM alloy, even if both basal $\langle a \rangle$ slip and prismatic $\langle a \rangle$ slip are activated, there is still no way to accommodate strains along the c -axis, although deformation twinning can help alleviate this problem. However, as mentioned above, deformation twins do not occur frequently in the ϵ -CCM alloy, except for in the grains with tensile orientations close to c -axis. Therefore, fracture frequently occurs at grain boundaries because of inhomogeneous deformation caused by the compatibility strain necessary for accommodating the shape and orientation changes in neighboring grains.

Hutchinson [30] took a theoretical approach to investigating the continuous plastic deformation in hcp metals and pointed out that continuous deformation through activation of only the $\langle a \rangle$ slip on the basal and prismatic planes is possible in the case of the hcp polycrystals with randomly oriented grains. This theoretical prediction supports the validity of our finding of continuous deformation of the polycrystalline ϵ -CCM alloy.

3-3. Dislocation accumulation at grain boundaries

3-3-1. Accumulation of geometrically necessary dislocations (GNDs)

There are only four independent strain components caused by activation of basal $\langle a \rangle$ slip and prismatic $\langle a \rangle$ slip. Therefore, the Von-Mises [31] criterion is not satisfied for homogeneous deformation in polycrystalline ϵ -CCM alloy.

A nonuniform plastic deformation is accompanied by the development of GNDs [32], which preserve the compatibility of the crystallographic lattice. GNDs are distinguished

from the so-called statistically stored dislocations (SSDs), which are responsible of the plastic flow carried by crystallographic slip along distinct slip planes.

There is a simple method for calculating the GND densities from EBSD-kernel average misorientation (KAM) data [5], which follows the method reported by Kubin and Mortensen [33]. According to Calcagnotto et al. [5], the KAM misorientation angle $\Delta\theta$ is related to the GND density ρ_{gnd} as in the following equation (3-1). This equation assumes a series of cylinder-torsion twist subgrain boundaries, each containing two perpendicular arrays of screw dislocations:

$$\rho_{gnd} = \frac{2\Delta\theta}{ub} \quad (\text{Eq. 3-1}),$$

where u is the unit length (step size in EBSD measurement (=0.5 μm in this work)) and b is magnitude of the Burgers vector.

As a first-order approach, the KAM, which is retrieved directly from the EBSD data, was chosen as a measure of local misorientations. The KAM quantifies the average misorientation around a measurement point with respect to a defined set of nearest or nearest plus second-nearest neighbor points. Values above a predefined threshold (here, it is 2°) are excluded from the calculation, because these points are assumed to belong to adjacent grains or subgrains.

Figure 5 shows the experimental results for the GND accumulation calculated by equation (3-1) using KAM data ((a) 0% strain and (b) 10% strain) and for the (c) crystallographic orientation parallel to the tensile axis before and after deformation for each grain. It also includes (d) a schematic illustration showing the magnitude of GND accumulation according to the result in (b). In Fig. 5(d), an increased thickness of the gray zone means that more GNDs are accumulated at the boundary. The number of GNDs is found to increase with increasing strain, and GNDs are found to accumulate at specific boundaries in Fig. 5(a) and 5(b). The inverse pole figure showing the change in tensile orientation of each grain before and after 10% deformation in Fig. 5(c) reveals that the crystallographic rotations in grains G2 and G5 are very large. Fig. 5(d) reveals that much more accumulation of GNDs occurs at the triple junction of grains G3, G2, and G6 and at the boundary between G3 and G2. In order to characterize the dependence of the types of grain boundaries and the orientation of each grain on GND accumulation and fracture, a crystal plasticity analysis was conducted to calculate the scale-dependent properties of the yield phenomena of polycrystals using continuum-mechanics-based crystal plasticity analyses [6-10], as follows.

3-3-2. GND accumulation in ϵ -CCM alloy determined by dislocation-model-based strain gradient crystal plasticity analysis

3-3-2-1. Models

This section explains the models used for evaluating the GND accumulation in our dislocation-model-based strain gradient crystal plasticity analysis. This calculation assumes infinitesimal deformation, and the maximum nominal strain was set to 10%. This model considers three active $\{0001\}\langle 11\bar{2}0\rangle$ slip systems (Nos. 1–3) and three active $\{1\bar{1}00\}\langle 11\bar{2}0\rangle$ slip systems (Nos. 4–6). The other slip systems on the pyramidal plane (Nos. 7–12) and the $\{1\bar{1}02\}$ twinning systems (Nos. 12–18) are assumed not to be activated; that is, their CRSS values are set extremely high (= 10 GPa) in the calculation. The activation condition of slip system n is given by the Schmid law as follows:

$$P_{ij}^{(n)}\sigma_{ij} = \theta^{(n)}, \quad P_{ij}^{(n)}\dot{\sigma}_{ij} = \dot{\theta}^{(n)} \quad (n = 1, \dots, 18) \quad (\text{Eq. 3-2, 3-3}),$$

$$\dot{\theta}^{(n)} = \sum_m h^{(nm)}\dot{\gamma}^{(m)} \quad (\text{Eq. 3-4}),$$

and

$$P_{ij}^{(n)} = \frac{1}{2}(v_i^{(n)}b_j^{(n)} + v_j^{(n)}b_i^{(n)}) \quad (\text{Eq. 3-5}),$$

where σ_{ij} and $\theta^{(n)}$ denote the stress and the critical resolved shear stress on slip system n , respectively. Symbols with a dot indicate increments in the corresponding parameters.

Furthermore, $v_i^{(n)}$ and $b_i^{(n)}$ are the slip plane normal and the slip direction, respectively, and they define the Schmid tensor $P_{ij}^{(n)}$. The $\dot{\theta}^{(n)}$ is the increment in the

critical shear stress, and $\dot{\gamma}^{(m)}$ denotes the increment in plastic shear strain on slip system m . The constitutive equation assuming the infinitesimal strain approximation is expressed as follows [34]:

$$\dot{\sigma}_{ij} = \left[S_{ijkl}^e + \sum_n \sum_m \{h^{(nm)}\}^{-1} P_{ij}^{(n)} P_{kl}^{(m)} \right]^{-1} \dot{\epsilon}_{kl} \quad (\text{Eq. 3-6}),$$

where S_{ijkl}^e denotes the elastic compliance. The summation is made over all active slip systems.

In crystal plasticity analyses, the critical resolved shear stress for slip system n has been

given by the modified Bailey–Hirsch model [6]:

$$\theta^{(n)} = \theta_0^{(n)} + \sum_n \Omega^{(nm)} a \mu \tilde{b} \sqrt{\rho_s^{(m)}} \quad (\text{Eq. 3-7}),$$

where the first term on the right side of Eq. (3-7) is the lattice friction stress for moving dislocations and the second term defines the slip resistance of SSDs on twelve slip systems against moving dislocations on slip system n . Furthermore, $\rho_s^{(m)}$ denotes the density of SSDs accumulated on slip system m , Ω gives the interaction matrix between slip systems, and a is a numerical factor of the order of 0.1.

The increment in the SSD density is given by

$$\dot{\rho}_s^{(n)} = c \dot{\gamma}^{(n)} / \tilde{b} L^{(n)} \quad (\text{Eq. 3-8}),$$

where c is a numerical constant of the order of 1, respectively. Furthermore, $L^{(n)}$ is the mean free path of moving dislocations on slip system n and is defined by Ohashi [9] as

$$L^{(n)} = \frac{c^*}{\sqrt{\sum_m \omega^{(nm)} (\rho_s^{(m)} + \|\rho_G^{(m)}\|)}} \quad (\text{Eq. 3-9}),$$

where c^* is a numerical constant of the order of 10–100. Here, $\|\rho_G^{(m)}\|$ denotes the density norm of GNDs on slip system m and is defined as follows [7]:

$$\|\rho_G^{(n)}\| = \sqrt{(\rho_{G,edge}^{(n)})^2 + (\rho_{G,screw}^{(n)})^2} \quad (\text{Eq. 3-10}),$$

where $\rho_{G,edge}^{(n)}$ and $\rho_{G,screw}^{(n)}$ denote the edge and screw components of the GNDs on slip system n and are defined as

$$\rho_{G,edge}^{(n)} = -\frac{1}{\tilde{b}} \frac{\partial \gamma^{(n)}}{\partial \xi^{(n)}} \quad (\text{Eq. 3-11}), \quad \rho_{G,screw}^{(n)} = -\frac{1}{\tilde{b}} \frac{\partial \gamma^{(n)}}{\partial \zeta^{(n)}} \quad (\text{Eq. 3-12}).$$

Here, $\xi^{(n)}$ and $\zeta^{(n)}$ denote the directions parallel and perpendicular to the slip direction on the slip plane, respectively. The weight matrix $\omega^{(nm)}$ controls the contributions of accumulated SSDs and GNDs on slip system m to the mean free path of moving dislocations on slip system n . We assume that dislocations accumulated on the

slip planes of the moving dislocations do not contribute to the mean free path ($\omega^{(nm)} = 0$) and that all the other dislocations contribute equally ($\omega^{(nm)} = 1$). Details of the dislocation models are given elsewhere [9].

Evaluation of the edge and screw components of the GNDs enables one to calculate the tangent vector $\mathbf{I}^{(n)}$ of the dislocation line segments [6] as

$$\mathbf{I}^{(n)} = \frac{1}{\|\rho_G^{(n)}\|} (\rho_{G,screw}^{(n)} \mathbf{b}^{(n)} + \rho_{G,edge}^{(n)} \mathbf{b}^{(n)} \times \mathbf{v}^{(n)}) \quad (\text{Eq. 3-13})$$

and the characteristic angle φ of the dislocation segment as

$$\cos \varphi^{(n)} = \frac{\rho_{G,screw}^{(n)}}{\|\rho_G^{(n)}\|} \quad (\text{Eq. 3-14}), \quad \sin \varphi^{(n)} = \frac{\rho_{G,edge}^{(n)}}{\|\rho_G^{(n)}\|} \quad (\text{Eq. 3-15}).$$

Positive and negative edge dislocation segments have the characteristic angles $\pi/2$ and $3\pi/2$, respectively, while positive and negative screw segments have the characteristic angles 0 and π . We can visualize the distribution of GND segments with equations (3-13), (3-14), and (3-15) [9,10].

3-3-2-2. Data used for the numerical analysis

Figure 6(a) shows the finite-element mesh used for the numerical analysis. The dimensions of each element are $4 \mu\text{m} \times 4 \mu\text{m} \times 4 \mu\text{m}$, and the specimen is divided into $10 \times 20 \times 2$ elements in the x , y , and z directions, respectively. These elements are composite-type brick elements with eight nodes. The sample is meshed in a uniform manner in the x and y directions, which enables us to follow possible sharp changes in physical quantities around the grain boundaries and sample surfaces. A class of grain structures is employed, as shown in Fig. 6(b). These grain structures are shown to be similar to the microstructure of the ε -CCM sample in Fig. 5(a). Herein, the tensile axis is the y -axis. The parameters used in the simulation are shown in Table 1. The lattice friction stresses ($\theta_0^{(n)}$) were set to 211 MPa for prismatic $\langle a \rangle$ slip ($n=4, 5$ or 6) and 184 MPa for basal $\langle a \rangle$ slip ($n=1, 2$ or 3); these stresses were identified experimentally as discussed in section 3-2-2. The lattice friction stresses for other slip systems ($n=7-12$) and twinning systems ($n=13-18$) were set to 10 GPa, meaning that these slip systems and twinning systems are assumed not to be activated. Therefore, this simulation

considers the following six slip systems: the $(0001)[11\bar{2}0]$, $(0001)[\bar{1}2\bar{1}0]$, $(0001)[\bar{2}110]$, $(1\bar{1}00)[11\bar{2}0]$, $(10\bar{1}0)[\bar{1}2\bar{1}0]$, and $(01\bar{1}0)[\bar{2}110]$ slip systems. The initial dislocation density on each slip system ρ_0 is set to be $1.0 \times 10^{10} \text{ (m}^{-2}\text{)}$.

3-3-2-3. Dislocation accumulation and distributions of local stress and local strain (experimental and numerical results)

Figure 7(a-d) shows numerical results for the density norm of the GNDs on each slip system after deformation at a strain of 10%. The accumulation of GNDs is found to be concentrated at boundaries or triple junctions of boundaries. There is no apparent accumulation of GNDs on slip systems of $(0001)[\bar{1}2\bar{1}0]$ and $(0001)[\bar{2}110]$, therefore, the results of these slip systems are not shown. The density norm of GNDs in the $(1\bar{1}00)[11\bar{2}0]$ slip system is concentrated at the G6 side in the vicinity of the G3-G6 boundary. The density norm of GNDs in the $(10\bar{1}0)[\bar{1}2\bar{1}0]$ slip system is concentrated at the G6 side in the vicinity of the G6-G2 boundary and in the vicinity of the triple junction between G6, G5, and G2. The density norm of GNDs in the $(01\bar{1}0)[\bar{2}110]$ slip system is concentrated at the G2 side of triple junction between G3, G2, and G6, and, finally, the density norm of GNDs in the $(0001)[11\bar{2}0]$ basal slip system is concentrated at the G3 side of the triple junction between G3, G6, and G2 and inside grain G5. Although the constraining effects of other surrounding grains and the shape of the boundary should be considered in this simulation in order to characterize the experimental results more closely, the calculated accumulation of GNDs in Fig. 7(a-d) is found to be quite consistent with the experimental result (Fig. 5). Figure 7(e-h) shows the distributions of SSDs, and it would be discussed in later.

In order to understand the distributions of simulated GNDs more clearly, the results of Figs. 7(a)-(d) are summarized in one figure of Fig. 8(a). In Fig. 8(a), the respective simulated result (in Figs. 7(a)-(d)) is drawn in the experimental result of Fig. 5(d). We can clearly distinguish the GNDs' character at each boundary according to the simulation result. Large, complicated accumulations of GNDs are seen at the triple junction between G3, G2, and G6, indicating that a high internal stress is accumulated in the vicinity of this triple junction. In fact, when the tensile orientations of G3, G2, and G6 (as shown in Fig. 5(c)) are considered, the anisotropic deformation due to incompatibility at the grain boundaries is expected to be high at this triple junction. This simulation also makes it possible to predict the dislocation type. Figure 8(b) shows a summary of the types of GNDs according to the equations of (3-11) and (3-12) in the experimental result of Fig. 5(d), indicating that various kinds of dislocations exist.

During plastic deformation, GNDs are required to maintain the lattice continuity, and

SSDs evolve from random trapping processes. Figure 7(e-h) shows the distributions of the SSDs of the (e) $(1\bar{1}00)[11\bar{2}0]$, (f) $(10\bar{1}0)[\bar{1}2\bar{1}0]$, (g) $(01\bar{1}0)[\bar{2}110]$, and (h) $(0001)[11\bar{2}0]$ slip systems after tensile deformation at a strain of 10%. A large accumulation of SSDs in the $(1\bar{1}00)[11\bar{2}0]$ slip system is seen at a central location of G6 grain (Fig. 7(e)), while the GNDs are accumulated at the G3-G6 boundary (Fig. 7(a)). The accumulation of SSDs can be estimated from the magnitude of the slip strain and dislocation mean free path (in equation (3-8)). Figures 8(c) and 8(d) show the distribution of strain YY (ε_{YY}) and the distribution of stress YY (σ_{YY}) at a tensile strain of 10%, respectively. This distribution of SSDs (Fig. 7(e)) is similar to the distribution of the ε_{YY} strain component, indicating that the accumulation of SSDs in the $(1\bar{1}00)[11\bar{2}0]$ slip system is simply led by evolution of the plastic strain ε_{YY} (Fig. 8(c)). On the other hand, it can be noted that interestingly, the SSDs in the $(10\bar{1}0)[\bar{1}2\bar{1}0]$ slip system accumulate at the boundaries (Fig. 7(f)), and the density of SSDs is extremely high at the G6 side in the vicinity of the triple junction between G2, G6, and G5. This SSD density is different from the distribution of the strain ε_{YY} (Fig. 8(c)). The SSD density in the $(01\bar{1}0)[\bar{2}110]$ slip system (Fig. 7(g)) shows a large accumulation at triple junction between G3, G2, and G6, which is similar to the density of GNDs (Fig. 7(c)). The accumulated GNDs are supposed to act as forest dislocations to obstruct the movement of dislocations, resulting in a shortening of the mean free path, as stated in equation (3-9). This fact has been pointed out by Ohashi et al. [35]. A GND accumulation is seen at the G2-G6 boundary in the $(10\bar{1}0)[\bar{1}2\bar{1}0]$ slip system (Fig. 7(b)), so it can be expected that the large GND accumulation in the $(10\bar{1}0)[\bar{1}2\bar{1}0]$ slip system leads to shortening of the mean free paths of moving dislocations in slip systems with slip planes intersecting with that of the present $(10\bar{1}0)[\bar{1}2\bar{1}0]$ slip system. Meanwhile, according to the GND distributions in Fig. 7(a-d), the extremely large SSD accumulation at the triple junction between G2, G6, and G5 in Fig. 7(f) is thought to arise from a combination of interactions among GNDs in the $(1\bar{1}00)[11\bar{2}0]$, $(10\bar{1}0)[\bar{1}2\bar{1}0]$, and $(0001)[11\bar{2}0]$ slip systems. In addition, it can be noted that SSD accumulation in the $(0001)[11\bar{2}0]$ slip system is very small in G3 (Fig. 7(h)), although a large GND accumulation in the $(0001)[11\bar{2}0]$ slip system is seen at triple junction between G3, G2, and G6. This result indicates that the GNDs in the $(0001)[11\bar{2}0]$ slip system are developed from incompatibility strains due to large misorientation at the grain boundaries. In fact, there are quite different tensile orientations among the G1, G2, G3, and G6 grains, so high incompatibility strains should arise at these grain boundaries. This incompatibility indicates highly localized plastic deformation near boundaries.

Deformation is found to be concentrated in grains G2 and G6 (Figs. 8(c) and 8(d)),

which have plastic strains ε_{YY} of more than 14%. The strains ε_{YY} are the highest in the central regions and exhibit a gradient in grains G2 and G6. The distribution of stress YY (σ_{YY}) in Fig. 8(d) reveals that the stress is ranging from 500 to 717 MPa inside all grains G1, G2, G3, G5, and G6, and the stress is around 850 MPa at boundaries at G1-G3, G2-G6, G5-G6 and G2-G6. This stress value at these boundaries is almost consistent with the experimental value of 875 MPa (at a strain of 10%) shown in Fig. 1(b). In contrast, an extremely high σ_{YY} of more than 1000 MPa is seen at the boundaries, and the highest value of 1150 MPa is exhibited in grain G3 in the vicinity of the G3-G2 grain boundary. This stress concentration at the boundaries is the result of a large accumulation of GNDs (as shown in Figs. 5, 7, and 8(a)) that are formed due to the plastic incompatibility at the boundaries. In addition, according to the summary of the GND distributions in Fig. 8(a), the region of concentrated stress at the G3-G2 boundary is found to arise from accumulation of GNDs in the $(0001)[11\bar{2}0]$ slip system. The stress-strain curve in Fig. 1(b) reveals that catastrophic fracture occurs at a stress of 1072 MPa, so the simulation result (Fig. 8(d)) implies that microcracking should be initiated at the grain boundary of G3-G2.

Next, the effect of the activation of both basal $\langle a \rangle$ slip and prismatic $\langle a \rangle$ slip on the relaxation of the stress concentration at the boundary is discussed. Figure 8 (e) shows the distribution of stress YY (σ_{YY}) after tensile deformation at 5% strain simulated without consideration of the prismatic $\langle a \rangle$ slip activity. That is, the calculation shown in Fig. 8(e) was conducted with extremely high CRSS values of 10 GPa for the prismatic $\langle a \rangle$ slip, so that this simulation considers only basal $\langle a \rangle$ slip activation. An extremely high stress σ_{YY} is found even at a tensile strain of 5%. Furthermore, the highest stress σ_{YY} of 1860 MPa is seen at the G1 side in the vicinity of the G1-G3 boundary. This result indicates that an extremely high stress concentration takes place at the boundary if the prismatic $\langle a \rangle$ slip cannot operate, so cracking and fracture at the boundary are expected to occur easily under these conditions. Comparison of the stress concentrations in Figs. 8(d) and 8(e) demonstrates that the activity of prismatic $\langle a \rangle$ slip in addition to basal $\langle a \rangle$ slip contributes to the relaxation of stress concentrations at the grain boundaries. This effect contributes to the excellent ductility of 38% obtained in the ε -CCM alloy, as shown in Fig. 1(b). In this study, no deformation twinning activity can be observed in the EBSD and TEM results, even at the grain boundaries, except in the case of grains with a tensile orientation close to the $[0001]$ axis. However, there is a possibility that deformation twinning is activated to accommodate stress concentrations in local areas in the vicinities of grain boundaries. According to the simulation results (Fig. 8), there are significantly high residual stresses at boundaries even at strain of 10%,

although the ϵ -CCM alloy exhibits high tensile ductility of 38 %. This result implies that twinning or $\langle c+a \rangle$ slip should be activate locally at boundaries in order to accommodate of c -axis strain. With respect to it, we need to carry out the detailed microstructural observation whether the deformation modes (twinning and $\langle c+a \rangle$ slip) to accommodate of c -axis strain are activated or not.

4. Summary

The microscopic mechanism of plastic deformation in a polycrystalline CCM alloy consisting of a single ϵ phase was examined using both an experimental approach and numerical analysis with a dislocation-model-based strain gradient crystal plasticity calculation. The polycrystalline ϵ -CCM alloy exhibits excellent tensile properties with a 0.2% proof stress of 630 MPa, an ultimate tensile stress of 1072 MPa, and an elongation to fracture of 38.3 %. The experimental results show that the dominant deformation mode is simultaneous activation of basal $\langle a \rangle$ slip and prismatic $\langle a \rangle$ slip. This simultaneous activation of both $\langle a \rangle$ slips is explainable in terms of the lattice constant ratio c/a of 1.610. On the other hand, there are few active deformation twins. During deformation, there is a tendency for the GNDs to accumulate at grain boundaries, and the magnitude of GND accumulation at a particular boundary depends on the character of the boundary. The obtained computer simulation result is found to be consistent with the experimental results. The type of GND (edge or screw) is also estimated in this simulation, and various types are found to accumulate at boundaries depending on the boundary character. Furthermore, this simulation reveals that the local stress values (σ_{YY}) in the vicinities of grain boundaries with high amounts of plastic incompatibility exceed the fracture stress of 1072 MPa in the ϵ -CCM alloy, even at a tensile strain of 10%. On the other hand, a simulation that considers the activation of only basal $\langle a \rangle$ slip reveals that the concentration of stress σ_{YY} at this boundary is more than 1800 MPa even at a tensile strain of 5%. These results indicate that the activity of prismatic $\langle a \rangle$ slip in addition to basal $\langle a \rangle$ slip would contribute to the stress relaxation at the boundaries, resulting in the excellent tensile ductility in the ϵ -CCM alloy.

References

- [1] A. Chiba, K. Kumagai, N. Nomura, S. Miyakawa: *Acta Mater.*, 55 (2007) 1309-1318.
- [2] A. Chiba, K. Kumagai, H. Takeda, N. Nomura: *Mater. Sci. Forum*, 475-479 (2005) 2317-2322.
- [3] S. Kurosu, H. Matsumoto, A. Chiba: *Metall. Mater. Trans.*, 41A (2010) 2613-2625.
- [4] H. Matsumoto, S. Kurosu, B.S. Lee, Y. Li, A. Chiba: *Scr. Mater.*, 63 (2010) 1092-1095.
- [5] M. Calcagnotto, D. Ponge, E. Demir, D. Raabe: *Mater. Sci. Eng.*, A527 (2010) 2783-2746.
- [6] T. Ohashi: *Phil. Mag.*, A70 (1994) 793-803.
- [7] T. Ohashi: *Phil. Mag. Lett.*, 75 (1997) 51-57.
- [8] T. Ohashi: *J. Phys. IV France*, 9 (1999) Pr9-279-284.
- [9] T. Ohashi: *Int. J. Plasticity*, 21 (2005) 2071-2088.
- [10] T. Ohashi, M Kawamukai, H. Zbib: *Int. J. Plasticity*, 23 (2007) 897-914.
- [11] T. Odahara, H. Matsumoto, A. Chiba: *Mater. Trans.*, 49 (2008) 1963-1969.
- [12] I.P. Jones, W.B. Hutchinson: *Acta Metall.*, 29 (1981) 951-968.
- [13] T. Nakano : Osaka University, private comm. (2012).
- [14] J.D. Eshelby: *Philos. Mag.*, 40 (1949) 903.
- [15] S. Boffi, G. Caglioti: *Energia Nucl.*, 20 (1973) 622.
- [16] A. Akhtar: *Metall. Trans.*, 6A (1975) 1105.
- [17] W. Betteridge: *Prog. Mater. Sci.*, 24 (1979) 51-142.
- [18] B.C. Wonsiewicz, W.A. Backofen: *Trans. Metal. Soc. AIME*, 239 (1967) 1422.
- [19] J. Koike, T. Kobayashi, T. Mukai, H. Watanabe, M. Suzuki, K. Maruyama, K. Higashi: *Acta Mater.*, 51 (2003) 2055-2065.
- [20] F.E. Hauser, P.R. Landon, J.E. Dorn: *Trans. ASM*, 50 (1958) 856-883.
- [21] A. Couret, D. Caillard: *Acta Metall.*, 33 (1985) 1447.
- [22] A. Couret, D. Caillard: *Acta Metall.*, 33 (1985) 1455.
- [23] A. Couret, D. Caillard: *J. Phys. III*, 1 (1991) 885-907.
- [24] S.R. Agnew, J.A. Horton, M.H. Yoo: *Metall. Mater. Trans.*, 33A (2002) 851-858.
- [25] J.W. Christian, S. Mahajan: *Prog. Mater. Sci.*, 39 (1995) 1.
- [26] K. Lu, N. Hansen: *Scr. Mater.*, 60 (2009) 1033.
- [27] M.H. Yoo: *Mater. Trans.*, 12A (1981) 409.
- [28] X.Y. Zhang, Y.T. Zhu, Q. Liu: *Scr. Mater.*, 63 (2010) 387-390.
- [29] N. Munroe, X. Tan: *Scr. Mater.*, 36 (1997) 1383-1386.
- [30] J.W. Hutchinson: *Metall. Trans.*, 8A (1977) 1465.

- [31] R. Von Mises: *Z. Angew. Math. Mech.*, 8 (1928) 161.
- [32] M.F. Ashby: *Philos. Mag.* 21, 1970, 399–424.
- [33] L.P. Kubin, A. Mortensen: *Scr. Mater.*, 48 (2003) 119-125.
- [34] R.Hill: *J. Mech. Phys. Solids*, 14 (1966) 95-102.
- [35] T. Ohashi, R.I. Barabash, J.W.L. Pang, G.E. Ice, O.M. Barabash: *Int. J. Plasticity*, 25 (2009) 920-941.

Figure captions

Figure 1 (a) EBSD-IQ maps of ϵ -CCM alloy at tensile strains of 0%, (b) nominal stress–nominal strain curve of ϵ -CCM alloy at room temperature and (c) EBSD-IQ maps of ϵ -CCM alloy at tensile strains of 6%.

Figure 2 (a-b) Inverse pole figures including counters denoting the Schmid factor (μ) of (a) basal $\langle a \rangle$ slip and (b) prismatic $\langle a \rangle$ slip. (c) Ratio of these Schmid factors for basal $\langle a \rangle$ slip and prismatic $\langle a \rangle$ slip. (d-e) Trace analysis results for slip planes of sample deformed at 6%.

Figure 3 (a) TEM bright-field image showing the dislocation substructure in a grain with a tensile orientation close to $[10\bar{1}0]$ after tensile deformation at a strain of 6%, (b) EBSD-OIM image of the ϵ -CCM alloy after tensile fracture showing the tensile orientation and (b) EBSD-grain boundary map in a grain with a tensile orientation close to $[0001]$. In (c), twin types are classified by line color.

Figure 4 SEM images ((a) lower magnification and (b) higher magnification) showing the fracture surface after deformation of ϵ -CCM alloy at a strain of 38 %.

Figure 5 GND distributions calculated by equation (3-4) at (a) 0% strain and (b) 10% strain. (c) Crystallographic orientation parallel to tensile axis before and after deformation for each grain. (d) Schematic illustration showing the magnitude of GND accumulation according to the result in (b).

Figure 6 (a) Finite-element mesh used for the numerical analysis. (b) grain structure employed in this work.

Figure 7 Calculated density norm of the GNDs in the (a) $(1\bar{1}00)[11\bar{2}0]$, (b) $(10\bar{1}0)[\bar{1}2\bar{1}0]$, (c) $(01\bar{1}0)[\bar{2}110]$, and (d) $(0001)[11\bar{2}0]$ slip systems, and calculated distributions of SSDs in the (e) $(1\bar{1}00)[11\bar{2}0]$, (f) $(10\bar{1}0)[\bar{1}2\bar{1}0]$, (g) $(01\bar{1}0)[\bar{2}110]$, and (h) $(0001)[11\bar{2}0]$ slip systems after tensile deformation at a strain of 10%.

Figure 8 (a) Summary of the character (slip system) of accumulated GNDs, (b) summary of the type (edge or screw) of accumulated GNDs. And calculated distributions of (c) strain YY (ϵ_{YY}), (d) stress YY (σ_{YY}) at a tensile strain of 10%, when activation of both basal $\langle a \rangle$ slip and prismatic $\langle a \rangle$ slip are considered and (e) calculated distribution of stress YY (σ_{YY}) at a tensile strain of 5% when only the basal $\langle a \rangle$ slip are considered.

Table 1 Material constants used for crystal plasticity analysis

Figure 1
[Click here to download high resolution image](#)

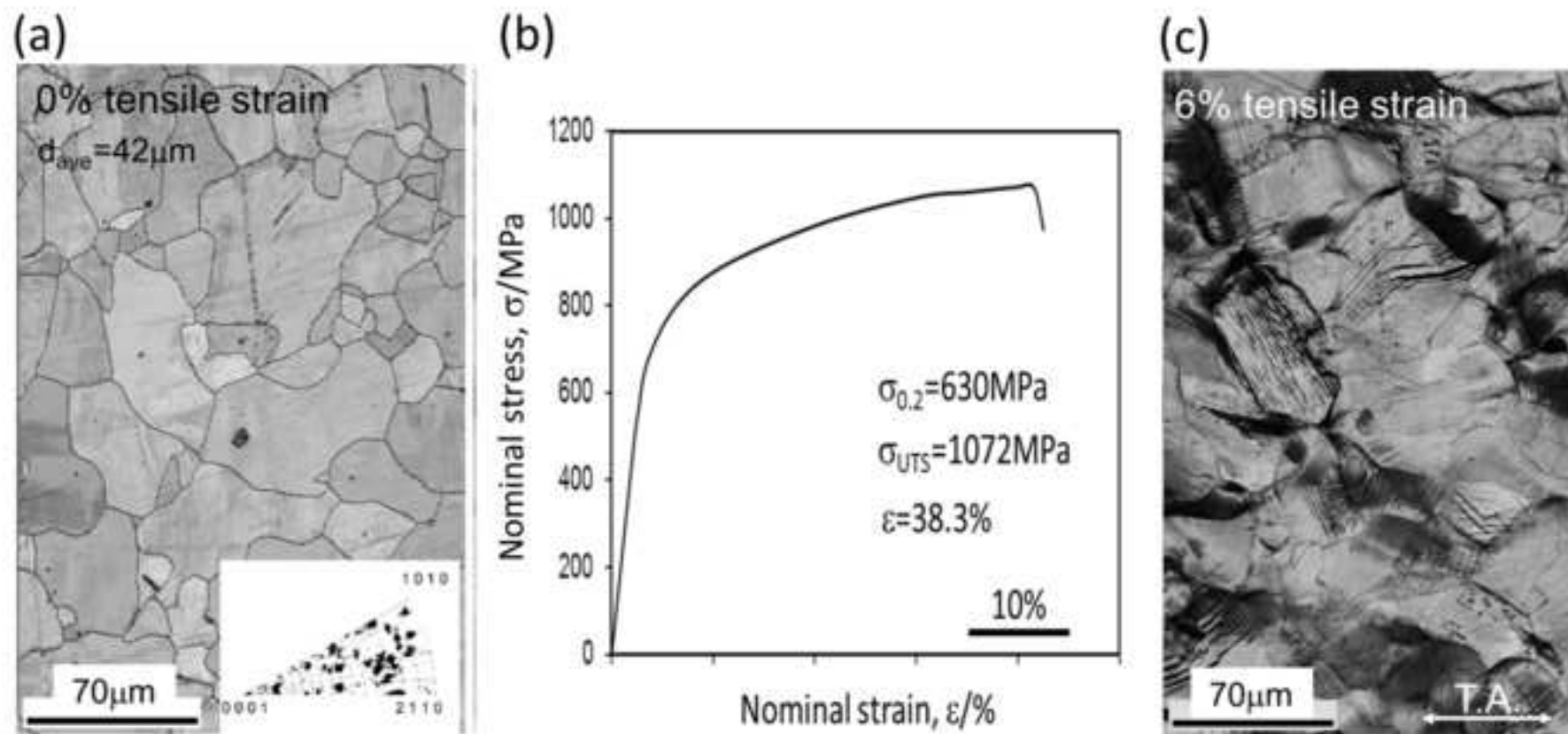


Figure 2
[Click here to download high resolution image](#)

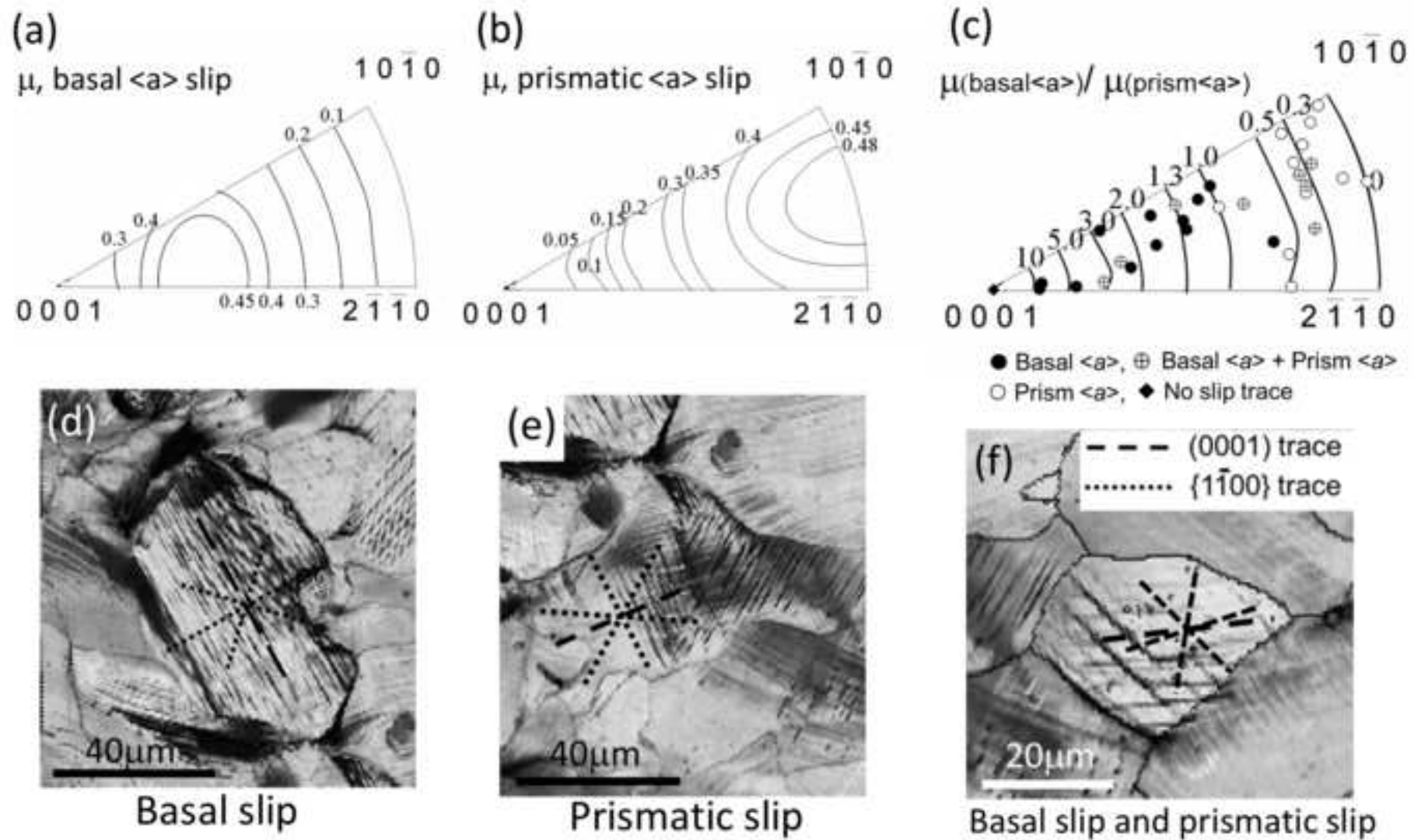


Figure 3
[Click here to download high resolution image](#)

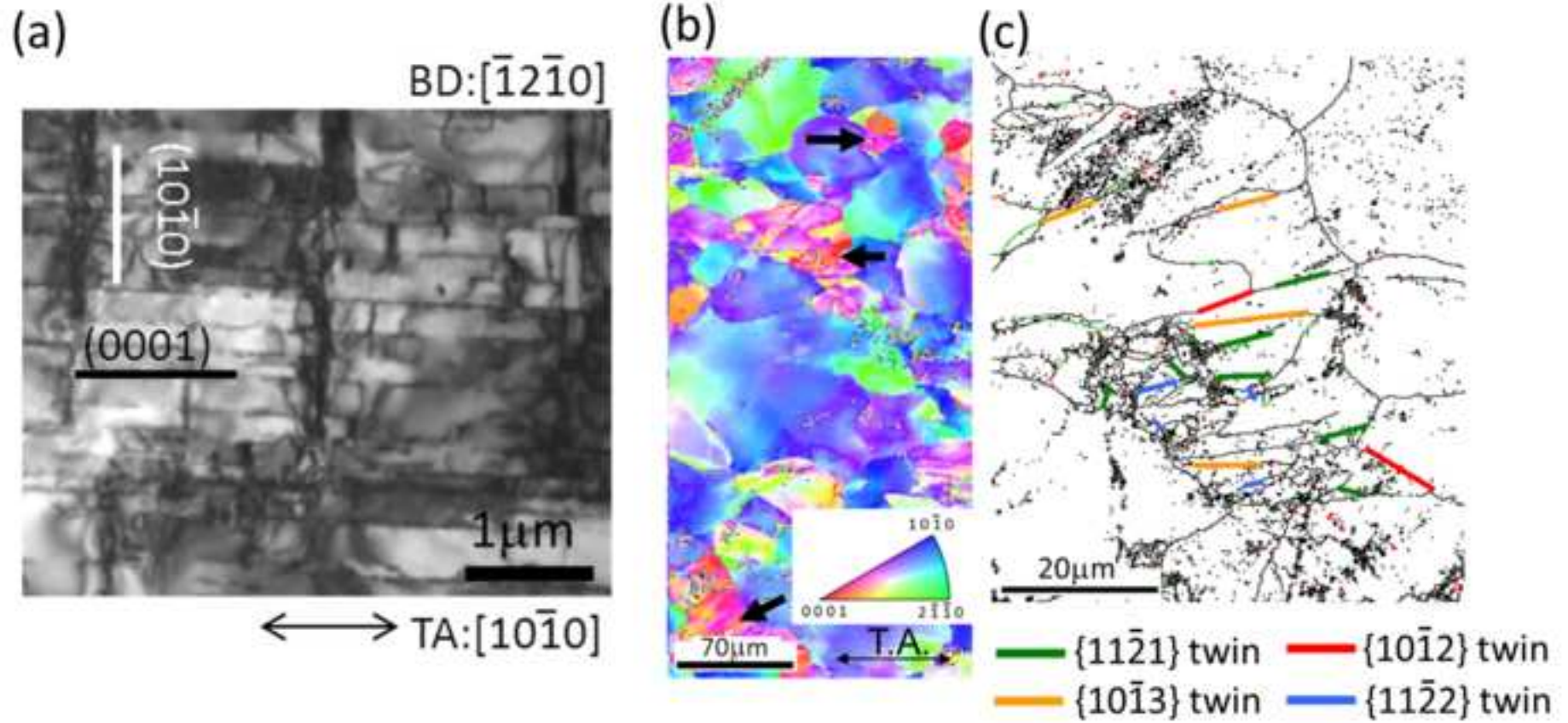


Figure 4
[Click here to download high resolution image](#)

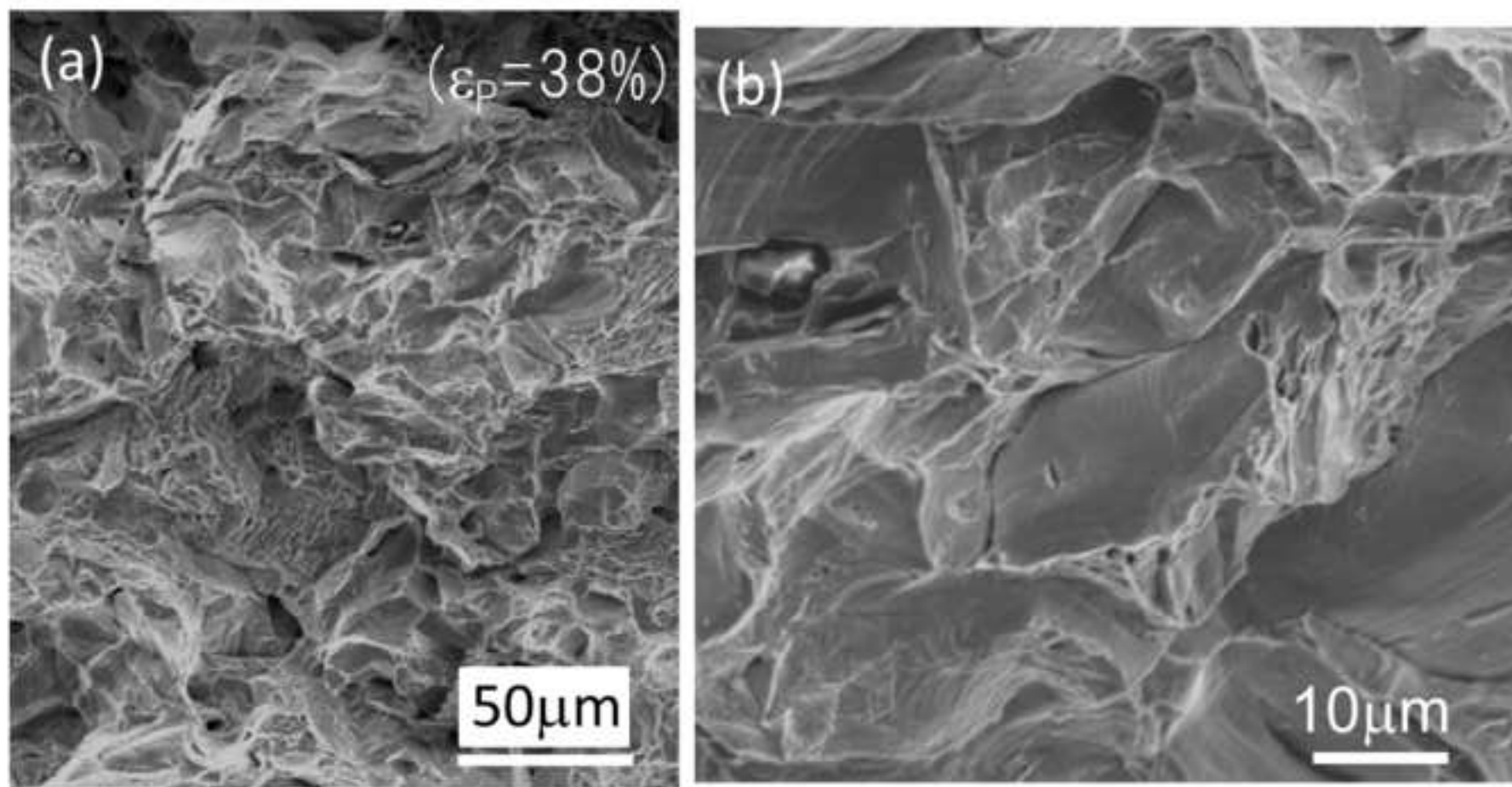


Figure 5
[Click here to download high resolution image](#)

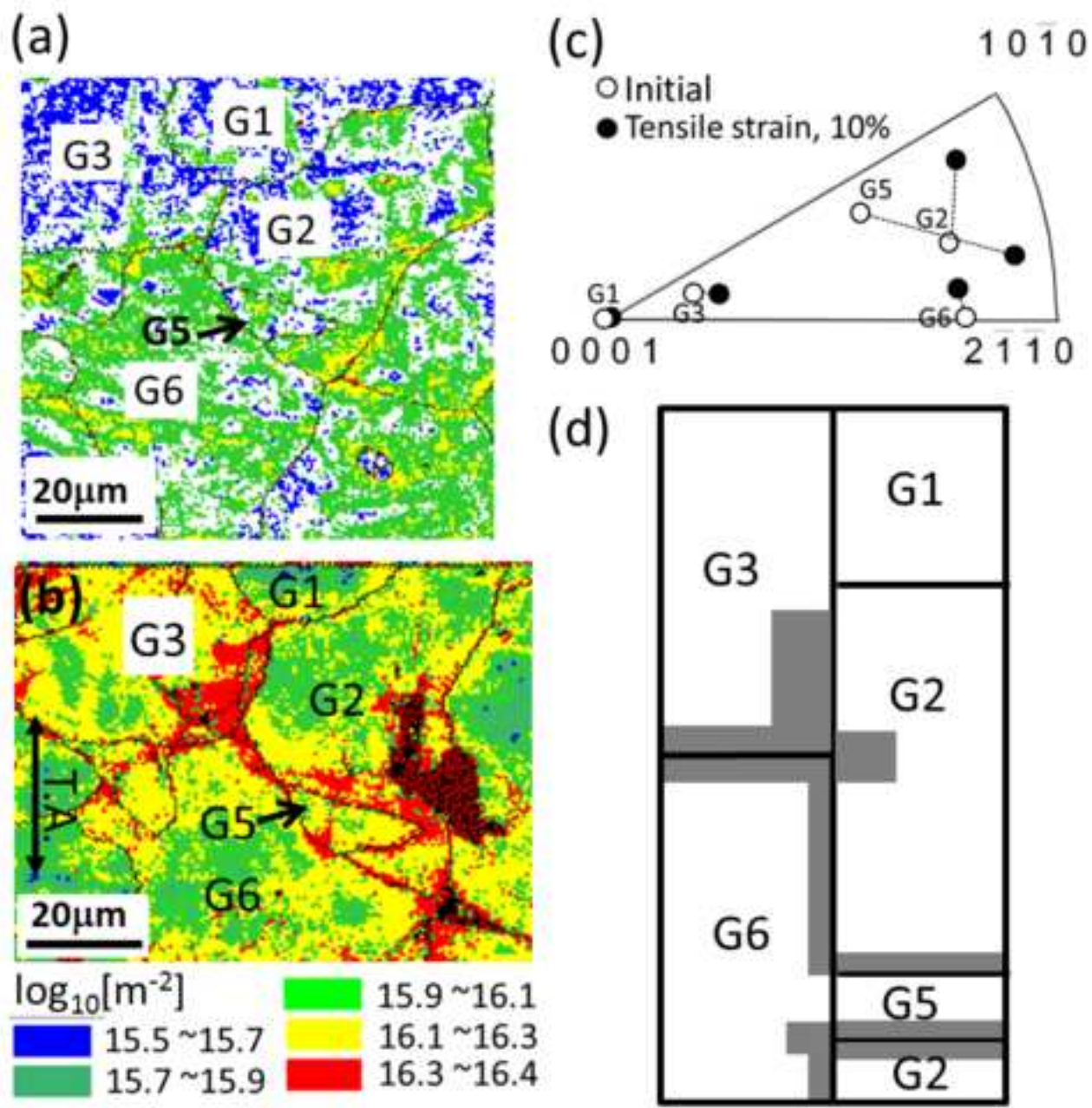


Figure 6
[Click here to download high resolution image](#)

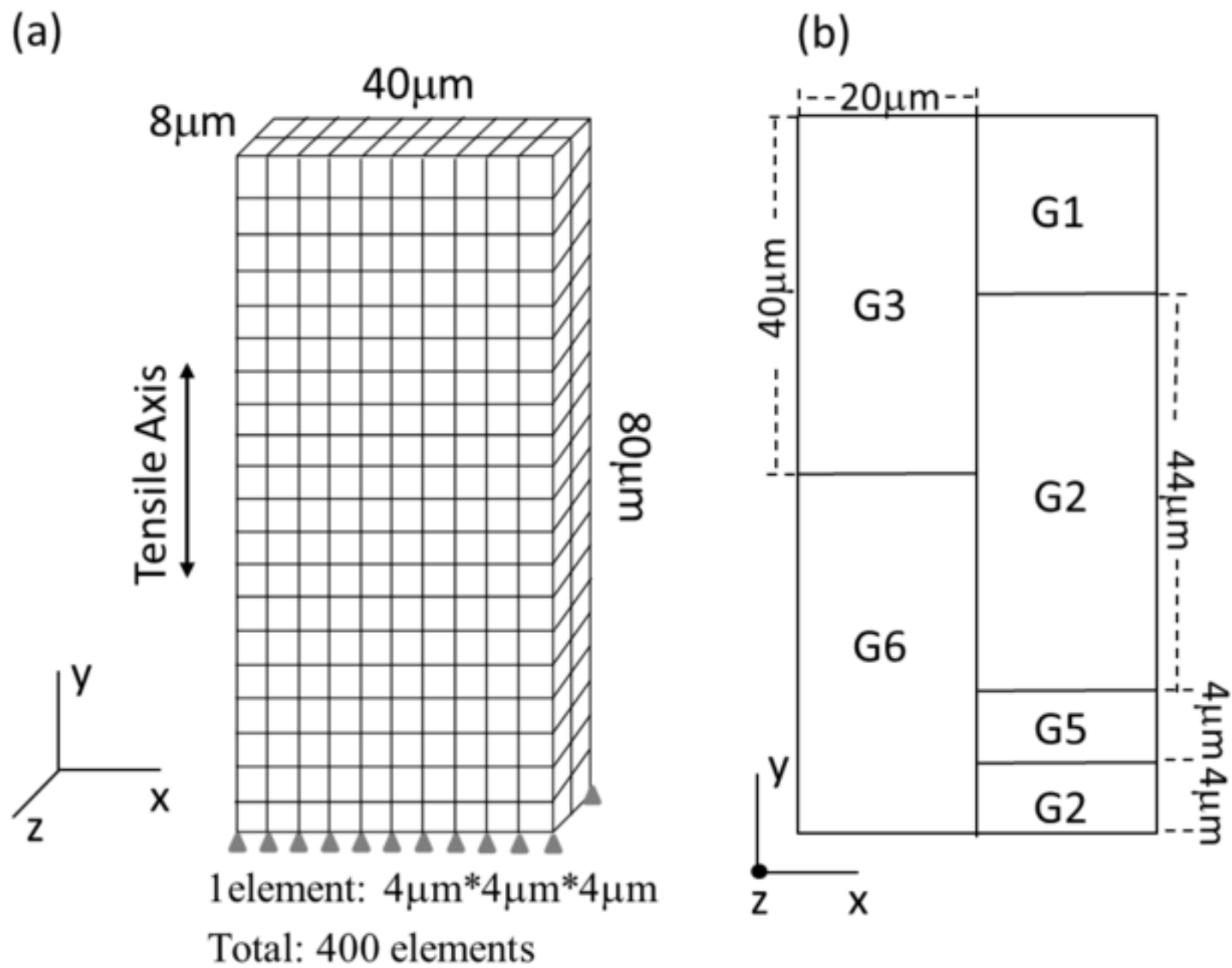


Figure 7
[Click here to download high resolution image](#)

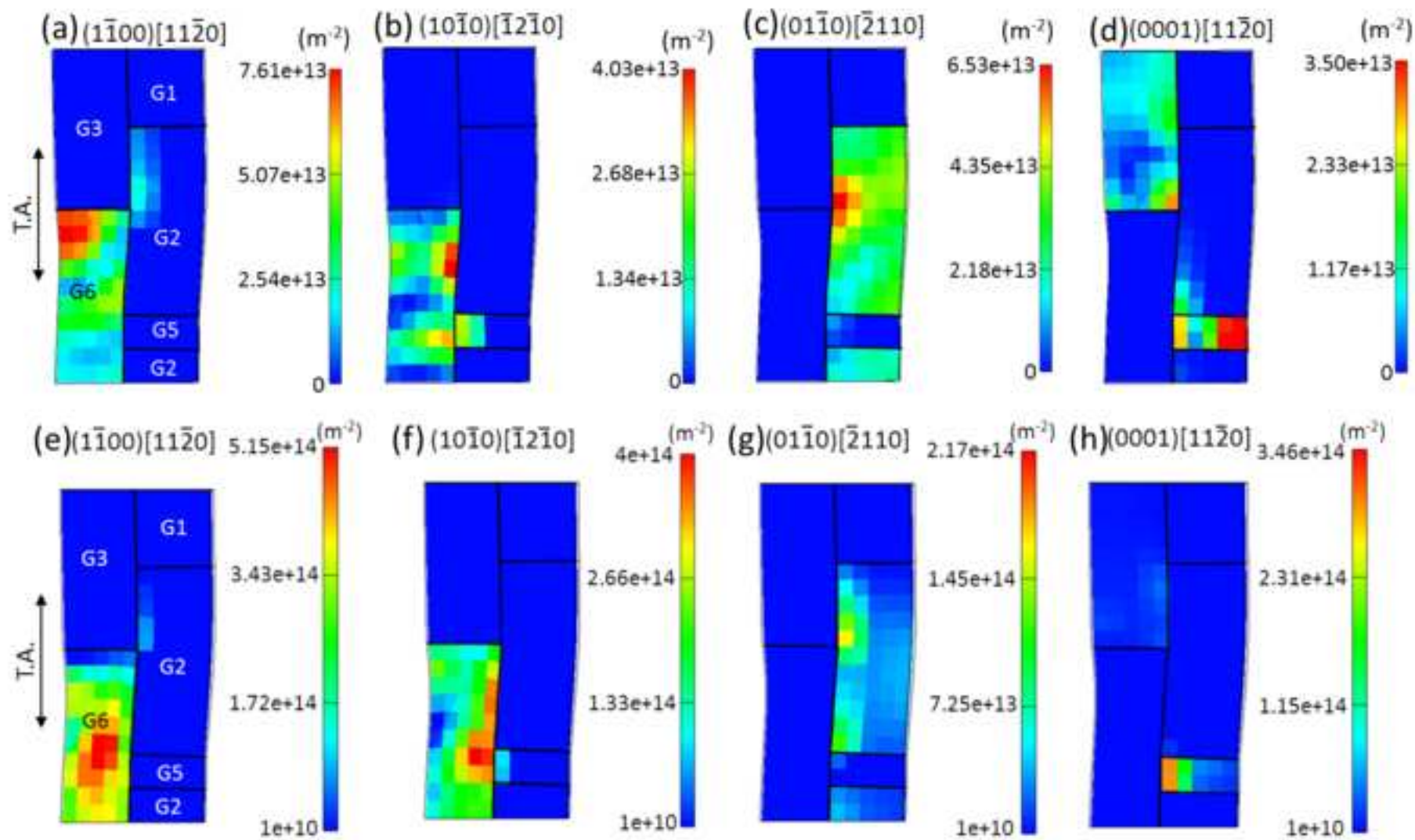


Figure 8
[Click here to download high resolution image](#)

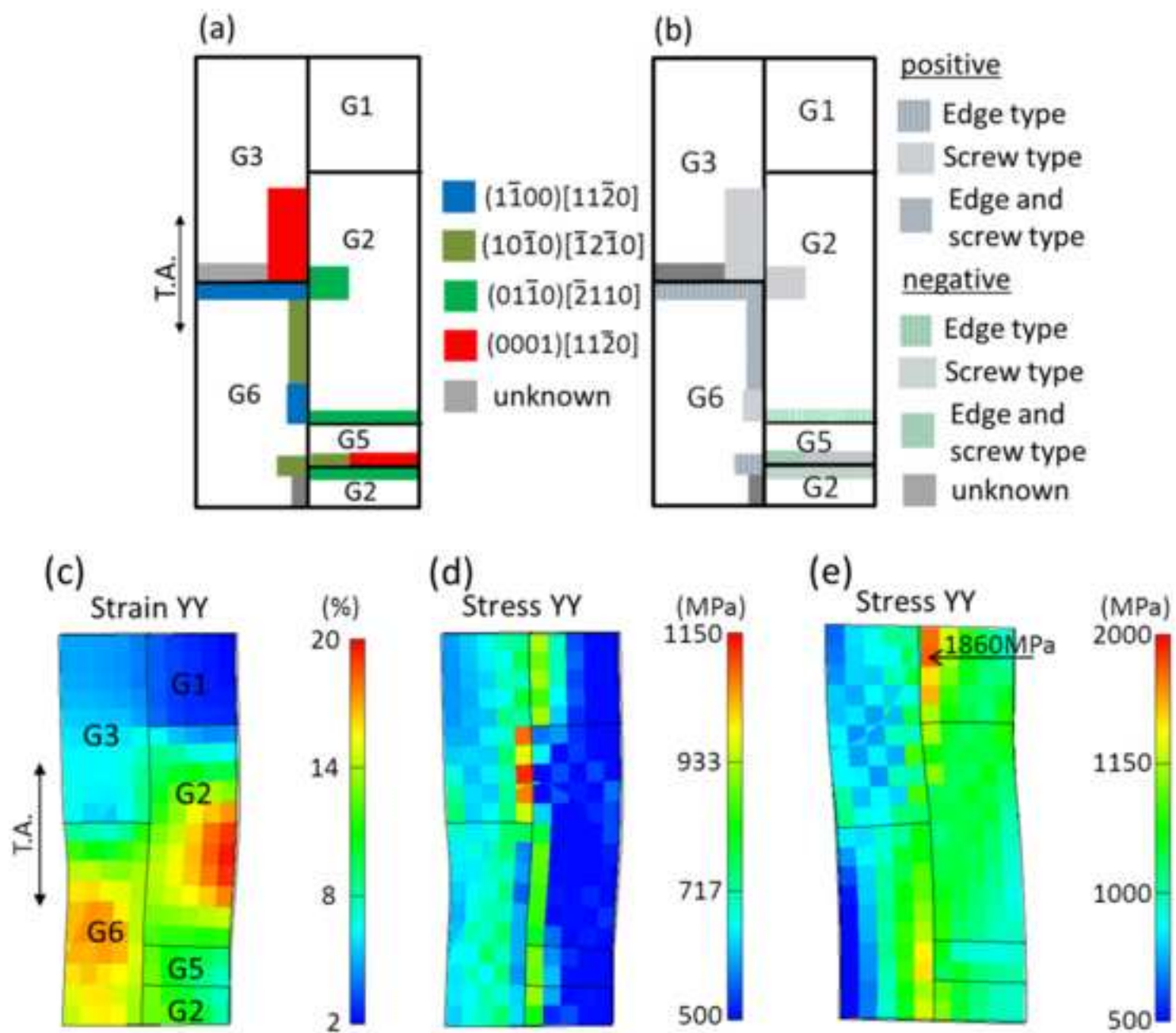


Table 1

[Click here to download high resolution image](#)

Elastic compliances, 10^{-11} Pa^{-1}	$s_{11}=0.4729, s_{12}=-0.2309,$ $s_{13}=-0.0694, s_{33}=0.3191,$ $s_{44}=1.3245$
a in (Eq 3-7)	0.1
c in (Eq 3-8)	1
c^* in (Eq 3-9)	15
Lattice friction stress θ_0 (basal slip), MPa	184
Lattice friction stress θ_0 (prismatic slip), MPa	211
Lattice friction stress θ_0 (other slip systems and twinning systems), GPa	10
Magnitude of the Burger's vector of $\langle a \rangle$ slip, \AA	2.5
Initial dislocation density, ρ_0 (m^{-2})	1.0×10^{10}